

AFD-STA: ADAPTIVE FILTERING DENOISING WITH SPATIOTEMPORAL ATTENTION FOR CHAOTIC SYSTEM PREDICTION

Chunlin Gong^{1,4}, Yin Wang^{2,3*}, Jingru Li⁵, Hanleran Zhang⁶

¹ University of Minnesota Twin Cities, Minneapolis, United States

² School of Statistics and Mathematics, Shandong University of Finance and Economics, Jinan, Shandong, China

³ Jinan Fengdi Intelligent Electronics Co., Ltd., Jinan, Shandong, China

⁴ Shandong Zhike Intelligence Computing Co., Ltd., Jinan, Shandong, China

⁵ School of Mechanical, Electrical and Information Engineering, Shandong University, Weihai, Shandong, China

⁶ SWUFE-UD Institute of Data Science, Southwestern University of Finance and Economics, Chengdu, Sichuan, China

ABSTRACT

This paper presents AFD-STA Net, a neural framework integrating adaptive filtering and spatiotemporal dynamics learning for predicting high-dimensional chaotic systems governed by partial differential equations. The architecture combines: 1) An adaptive exponential smoothing module with position-aware decay coefficients for robust attractor reconstruction, 2) Parallel attention mechanisms capturing cross-temporal and spatial dependencies, 3) Dynamic gated fusion of multiscale features, and 4) Deep projection networks with dimension-scaling capabilities. Numerical experiments on nonlinear PDE systems demonstrate the model's effectiveness in maintaining prediction accuracy under both smooth and strongly chaotic regimes while exhibiting noise tolerance through adaptive filtering. Component ablation studies confirm critical contributions from each module, particularly highlighting the essential role of spatiotemporal attention in learning complex dynamical interactions. The framework shows promising potential for real-world applications requiring simultaneous handling of measurement uncertainties and high-dimensional nonlinear dynamics.

Keywords Spatiotemporally chaotic system · Data-driven method · Filtering

1 Introduction

The translation of natural laws into theoretically grounded frameworks for engineering applications remains a core proposition in interdisciplinary research. Notably, even within deterministic systems, the sensitivity to initial conditions induced by strong nonlinear interactions leads to unpredictability in long-term evolutionary behaviors. Such dynamical systems that exhibit both determinism and unpredictability are collectively termed chaotic systems [1].

Research on chaotic systems has consistently attracted scholarly attention. Lorenz [2] demonstrated that minuscule variations in initial conditions could engender substantial divergence in outcomes. This stochastic variability and sensitivity to initial conditions established foundational understanding of chaotic systems. Ruelle and Takens [3] subsequently proposed the theory of strange attractors, characterizing chaotic systems through fractal dimensions and aperiodic orbits. Chen [4] extended the topological structure of Lorenz attractors, establishing the Chen chaotic model with more complex dynamical behaviors. At the partial differential equation level, the Kuramoto-Sivashinsky equation [5] successfully describes turbulent oscillatory dynamics in reaction-diffusion systems through spatiotemporal chaotic mechanisms. The Swift-Hohenberg equation [6] provides an effective chaotic modeling framework for pattern formation in crystal growth processes. The Brusselator equation [7] offers a robust framework for investigating self-

*Corresponding author: sduwangyin@163.com

organization and nonlinear phenomena in chemical reaction dynamics through its description of chemical oscillatory behaviors in reaction-diffusion processes.

Chaotic system prediction research has evolved two principal approaches: physics-based numerical methods and data-driven machine learning techniques. The former establishes explicit mathematical representations through differential equation systems [4, 5, 6, 7], solved via numerical discretization techniques such as spectral methods [8] and finite difference methods [9]. However, computational complexity typically escalates exponentially with dimensionality, and the construction of precise mathematical models heavily relies on domain-specific prior knowledge. The latter employs machine learning architectures like deep neural networks [10] to directly learn implicit evolutionary patterns from high-dimensional observational data, significantly reducing dependence on complete mechanistic models.

Current research presents numerous neural network applications for chaotic system prediction. Paper [11] proposed a temporal convolutional network incorporating spatial and channel attention mechanisms via convolutional block attention modules for chaotic systems and solar activity time series prediction. Study [12] developed an echo state network optimized through selective opposition grey wolf optimization for input weight matrix reconstruction and enhanced search capability, applied to Mackey-Glass and Lorenz chaotic system prediction. Work [13] introduced a hybrid architecture combining temporal convolutional networks with recurrent neural network layers for Lorenz system and arrhythmia ECG time series prediction. Research [14] presented a multifunctional recurrent fuzzy neural network integrating dual TSK fuzzy neural networks with feedback loops and particle swarm optimization, implemented in chaotic systems and industrial applications like gas furnace time series prediction. Investigation [15] combined long short-term memory networks with technical indicators (trend, momentum, volatility), employing Henry gas solubility optimization with logistic chaotic mapping for feature selection in WTI and Brent crude price prediction.

Our work focuses on data-driven neural network approaches for spatiotemporal chaotic system prediction. We employ phase space reconstruction to establish mapping relationships between delay attractors and original attractors, proposing a novel network architecture: AFD-STA.

- 1) Establishing diffeomorphic mapping relationships between delay attractors and original attractors based on Takens' embedding theorem, deriving rigorous mathematical characterizations for spatiotemporal information transformation
- 2) Proposing AFD-STA with a spatiotemporal attention gated fusion mechanism for decoupling and reconstructing multi-scale dynamical features

2 Preliminary

For PDE systems exhibiting complex spatiotemporal chaotic characteristics, the time-delay embedding theorem extracts the implicit manifold structure and establishes a topology-preserving mapping relationship from low-dimensional chaotic attractors to high-dimensional spatiotemporal patterns. This provides theoretical guarantees for embedding dynamical priors in subsequent machine learning models.

Takens embedding theorem [16] serves as a powerful tool for studying chaotic time series. The theorem states:

Theorem 1. *For an infinite-length, noise-free scalar time series $x(t)$ from a d -dimensional chaotic attractor, there exists an m -dimensional embedded phase space that preserves topological equivalence when $m \geq 2d + 1$.*

According to Takens embedding theorem, we can reconstruct the corresponding high-dimensional phase space from a one-dimensional chaotic time series, ensuring topological equivalence with the original system.

Typically, phase space reconstruction employs coordinate delay embedding, constructing phase space vectors through delay time τ and embedding dimension m :

$$X(t) = [x(t), x(t + \tau), x(t + 2\tau), \dots, x(t + (m - 1)\tau)] \quad (1)$$

where τ denotes the time delay and m represents the embedding dimension.

The generalized embedding theorem proposed by Deyle et al. [17] provides a methodology for attractor reconstruction using multivariate time series. Based on this theory, multivariate phase space vectors can be constructed to analyze intrinsic relationships between spatial variables. The embedding vector for multivariate time series can be defined as:

$$X(t) = [y_1(t), y_2(t), \dots, y_d(t), \dots, y_1(t + (m - 1)\tau), \dots, y_d(t + (m - 1)\tau)] \quad (2)$$

Building upon the generalized embedding theorem, Chen et al. [18] proposed an innovative method for reconstructing univariate time series attractors from high-dimensional time series:

Definition 1. Let O denote the observed system attractor with box dimension d_o . The time series $X(t_m) = [x_1(t_m), \dots, x_n(t_m)] \in \mathbb{R}^n$ represents the system state on O at time t_m , where $x_i(t_m)$ denotes the i -th component at the m -th time step. The delay coordinate map $\Psi : \mathbb{R}^n \rightarrow \mathbb{R}^{L+1}$ is defined as:

$$\Psi(X(t_m)) = [x_k(t_m), x_k(t_{m+1}), \dots, x_k(t_{m+L})] = Z(t_m) \quad (3)$$

where x_k represents our target variable of interest.

Combining the Equation (2) with Theorem 1, we obtain:

Theorem 2. Let O be the observed attractor with box dimension d_o , and L the future time step length for reconstruction. If L satisfies $L > 2d_o$, the reconstructed attractor $Z(t_m) = [x_k(t_m), x_k(t_{m+1}), \dots, x_k(t_{m+L})] \in \mathbb{R}^{L+1}$ from time series $X(t_m)$ maintains a topological conjugacy relationship with the original attractor O .

For a known m -dimensional time series $X(t_m)$ with M sampling points, the following mapping relationships exist:

$$\begin{cases} \Psi(X(t_m)) = Z(t_m), & m = 1, 2, \dots, M \\ \Phi(Z(t_m)) = X(t_m), & m = 1, 2, \dots, M \end{cases} \quad (4)$$

Considering that $Z(t_m)$ consists of $L + 1$ temporal components of x_k , Ψ can be expressed as a family of injective functions $\{\Psi_1, \Psi_2, \dots, \Psi_{L+1}\}$.

The matrix formulation reveals variable mapping relationships across different time steps:

$$\begin{pmatrix} \Psi_1(X(t_1)) & \Psi_1(X(t_2)) & \dots & \Psi_1(X(t_M)) \\ \Psi_2(X(t_1)) & \Psi_2(X(t_2)) & \dots & \Psi_2(X(t_M)) \\ \vdots & \vdots & & \vdots \\ \Psi_{L+1}(X(t_1)) & \Psi_{L+1}(X(t_2)) & \dots & \Psi_{L+1}(X(t_M)) \end{pmatrix} = \begin{pmatrix} x_k(t_1) & x_k(t_2) & \dots & x_k(t_M) \\ x_k(t_2) & x_k(t_3) & \dots & x_k(t_{M+1}) \\ \vdots & \vdots & & \vdots \\ x_k(t_{L+1}) & x_k(t_{L+2}) & \dots & x_k(t_{M+L}) \end{pmatrix} \quad (5)$$

This matrix formulation enables comprehensive capture of nonlinear relationships among multiple time series.

3 Methodology

3.1 AFD-STA Architecture

PDE systems are difficult to predict due to their spatiotemporal continuity and complex changing relationships. In this paper, we aim to learn system characteristics through discrete sampling points to predict unknown models. Consider an abstract infinite-dimensional system:

$$\frac{\partial u}{\partial t} = f(u; x).$$

where u is the unknown variable, and f is an arbitrary operator of any order or an arbitrarily complex linear or nonlinear function of u . Define the spatial interval as Δx , then $x_i = x_0 + i\Delta x, i = 1, \dots, D$. Similarly, we have $t_j = t_0 + j\Delta t, j = 1, 2, \dots$. Define $u_i^j = u(x_i, t_j)$, then:

$$u_i^j = g(U^0, U^1, \dots, U^j),$$

where $U^j = (u_1^j, u_2^j, \dots, u_D^j)$. Through spatiotemporal discretization, we obtain the independent variables $u_1^j, u_2^j, \dots, u_D^j$, and the original infinite-dimensional system is transformed into a D -dimensional dynamical system. Thus, the above formula can be regarded as the observed values of the original system.

Consider that our model aims to predict the delayed attractor $D = [x_k^{t_{M+1}}, \dots, x_k^{t_{M+L}}]$ at point x_k for L future steps by observing the original attractor $O = [U^{t_1}, U^{t_2}, \dots, U^{t_M}]^T$ composed of M observations of the original system. From Theorem 2, when the dimension d_o of the original attractor O satisfies $L \geq 2d_o + 1$, the delayed attractor D is topologically conjugate to the original attractor O . From Equation (1), the original attractor and the delayed attractor satisfy:

$$\begin{cases} \Psi(O) = D \\ \Phi(D) = O \end{cases}.$$

From the section 2, we can obtain the STI spatiotemporal information transformation equation for the original attractor and delayed attractor, as shown in Equation (5):

$$\begin{pmatrix} \Psi_1(U^{t_1}) & \Psi_1(U^{t_2}) & \cdots & \Psi_1(U^{t_M}) \\ \Psi_2(U^{t_1}) & \Psi_2(U^{t_2}) & \cdots & \Psi_2(U^{t_M}) \\ \vdots & \vdots & & \vdots \\ \Psi_{L+1}(U^{t_1}) & \Psi_{L+1}(U^{t_2}) & \cdots & \Psi_{L+1}(U^{t_M}) \end{pmatrix} = \begin{pmatrix} u_k^{t_1} & u_k^{t_2} & \cdots & u_k^{t_M} \\ u_k^{t_2} & u_k^{t_3} & \cdots & u_k^{t_{M+1}} \\ \vdots & \vdots & & \vdots \\ u_k^{t_{L+1}} & u_k^{t_{L+2}} & \cdots & u_k^{t_{M+L}} \end{pmatrix}.$$

Next, we construct a suitable neural network model to fit the nonlinear mapping Ψ . As shown in Figure 1, we design the AFD-STA Net as a nonlinear fitting neural network. To address the noise impact from the real world, a common solution is to use EWMA for data filtering. Our model introduces adaptive parameters on top of EWMA, proposing the Adap-EWMA module. AFD-STA first applies the Adap-EWMA module to the observed original attractor $O \in \mathbb{R}^{N \times M}$ for data smoothing, obtaining $H \in \mathbb{R}^{N \times M}$. To handle the influence of the remaining time series information of a node on its value at the current time, we use the Temporal-Attention module to expand the features of each time step and extract and fuse features from other time steps via the Self-Attention mechanism, obtaining $T \in \mathbb{R}^{M \times N \times \text{hidden}}$. Meanwhile, to measure the influence of other points in the system on the target point, we use the Spatio-Attention module to expand the features of each spatial point and perform feature extraction and fusion, obtaining $S \in \mathbb{R}^{N \times M \times \text{hidden}}$. The Fusion module employs a gated fusion mechanism to dynamically weight and fuse temporal and spatial feature information, followed by feature compression, yielding $F \in \mathbb{R}^{N \times M}$. Finally, we use a six-layer fully connected network (DynaFC6) to construct a deep mapping from spatiotemporal features to the delayed attractor. This network effectively extracts temporal dynamic features through intermediate layer upscaling-downscaling operations and captures the complex evolution patterns of the attractor using deep nonlinear transformations. In particular, the residual connection design maintains feature representation capability while ensuring training stability. Figure 2 illustrates the matrix dimension changes under each module's processing.

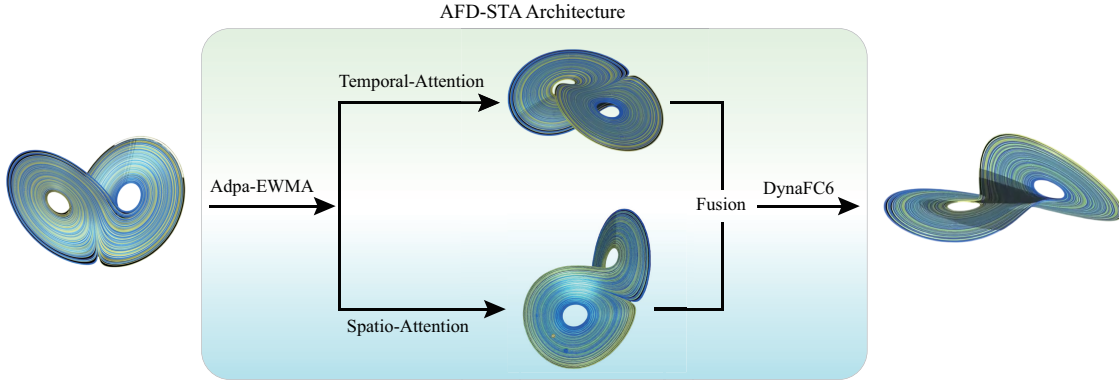


Figure 1: Demonstrates the overall strcuture.

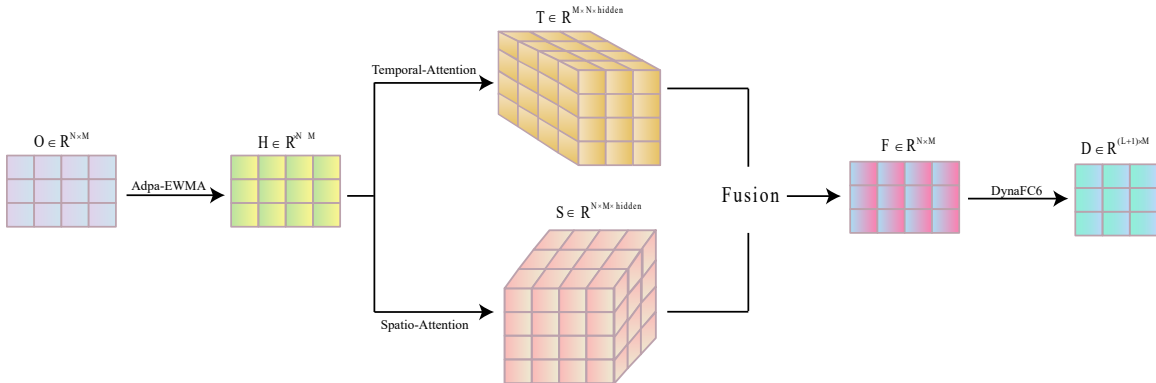


Figure 2: Demonstrates the the matrix dimension changes under each module's processing.

3.2 Adap-EWMA

The Exponential Weighted Moving Average (EWMA) [19] refers to a moving average with exponentially decreasing weights, where the weights of data points decrease exponentially over time, with more recent data weighted more heavily, but older data still given some weight. The EWMA method performs well in application scenarios with real-world noise, but its fixed decay parameters and decay rate make it difficult for the model to learn the noise characteristics of the current system. Considering that adjusting the decay coefficients for each position adaptively would require more training data and slower convergence, while fully data-driven decay coefficients for each time step may lead to poor interpretability and unstable results, this section introduces a learnable parameter as the baseline parameter, setting the position encoding as the decay rate. Through the learnable baseline parameter β and the decay rate, we can obtain different decay coefficients for each time step. This method extracts the dynamic trends of the original attractor O to achieve data denoising.

Nonlinear systems typically become progressively unstable over time, in which case we rely more on new observation data. Therefore, we stipulate that the position encoding increases, meaning later positions have greater weights. Define the position encoding vector $j = [0, 1, \dots, M-1] \in \mathbb{R}^M$, and introduce the learnable parameter β , obtaining the scaled intermediate vector h :

$$h = \beta \cdot j \in \mathbb{R}^M.$$

Through the sigmoid function, each element in h is mapped to a smoothing coefficient vector:

$$\alpha_j = \sigma(h_j) = \frac{1}{1 + e^{-h_j}} \in (0, 1), \quad \forall j \in \{0, \dots, M-1\}.$$

This yields $\alpha = [\alpha_0, \alpha_1, \dots, \alpha_{M-1}] \in \mathbb{R}^M$. The smoothed data H is initialized to zero and updated iteratively per time step. For the j -th time step of the i -th point, the current smoothed data $H(i, j)$ is computed by mixing the current observation $O(i, j)$ with the historical smoothed data $H(i, j-1)$:

$$H(i, j) = \alpha_j \times O(i, j) + (1 - \alpha_j) \times H(i, j-1),$$

This process can be expanded into an explicit weighted sum form:

$$H(i, j) = \sum_{k=0}^j \left(\alpha_k \prod_{l=k+1}^j (1 - \alpha_l) \right) O(i, j),$$

where the weight parameters satisfy the normalization constraint $\sum_{k=0}^j \alpha_k \prod_{l=k+1}^j (1 - \alpha_l) = 1 - \prod_{l=0}^j (1 - \alpha_l)$. When $\alpha_j \equiv \alpha$ is a constant, the formula degenerates into the standard EWMA form:

$$H(i, j) = \alpha \sum_{k=0}^j (1 - \alpha)^{j-k} O(i, j).$$

Through this method, we obtain the sequence for the same point $H^i = [H(i, 0), H(i, 1), \dots, H(i, M-1)]$, and extend the same process to different points to obtain $H = [H^1, H^2, \dots, H^N]^T \in \mathbb{R}^{N \times M}$.

3.3 Temporal-Attention and Spatio-Attention Module

Self-Attention [20] is widely used in LLMs due to its excellent ability to identify correlations within sequences. As shown in Figure 3, unlike the conventional application of Self-Attention to our time series, we use parallel temporal and spatial attention mechanisms. This approach not only considers the influence of a point at different times on its value at other times but also accounts for the mutual influence between points at the same time. For the previous step's $H \in \mathbb{R}^{N \times M}$, we first perform dimensionality expansion on the original matrix, then expand the features of each time step, obtaining the matrix $H' \in \mathbb{R}^{N \times M \times \text{hidden}}$. To account for the impact of different temporal and spatial positions on the model, we introduce randomly initialized, learnable temporal and spatial embedding matrices $T_{\text{pos}} \in \mathbb{R}^{1 \times M \times \text{hidden}}$, $S_{\text{pos}} \in \mathbb{R}^{N \times 1 \times \text{hidden}}$, and obtain H_τ through broadcasting:

$$H_\tau = H' \oplus T_{\text{pos}} \oplus S_{\text{pos}} \in \mathbb{R}^{N \times M \times \text{hidden}}.$$

Considering the Self-Attention calculation of mutual influences between variables in the first dimension, we pass $H_\tau \in \mathbb{R}^{N \times M \times \text{hidden}}$ into spatial attention to compute the mutual influence among N points. Transposing the first and second dimensions of H_τ yields $M \in \mathbb{R}^{M \times N \times \text{hidden}}$, which is passed into temporal attention to focus on computing mutual influences between time steps. The two matrices are processed through two independent single-head Self-Attention layers to compute:

$$S = \text{Spatio-Attention}(H_\tau) \in \mathbb{R}^{N \times M \times \text{hidden}},$$

$$T = \text{Temporal-Attention}(H'_T) \in \mathbb{R}^{M \times N \times \text{hidden}}.$$

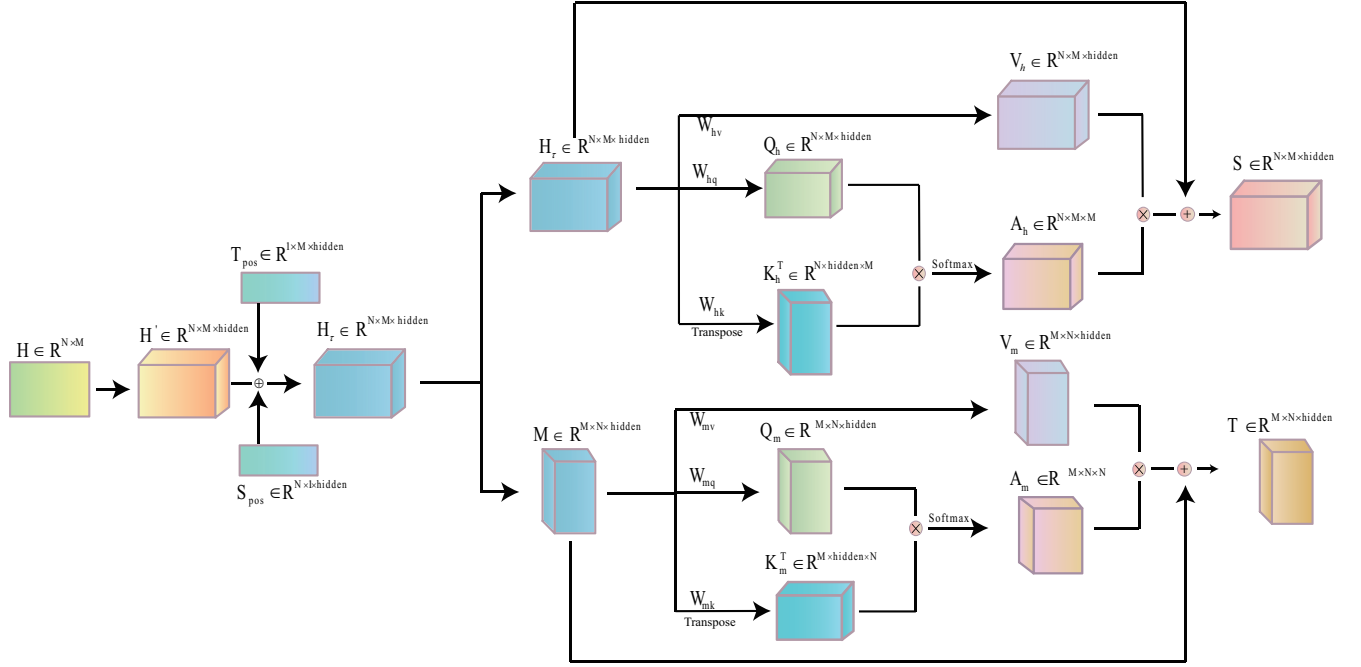


Figure 3: Spatiotemporal attention architecture

3.4 Fusion Module

In scenarios involving information aggregation under multiple parallel paths, dynamic weight control methods dominated by gating mechanisms have become mainstream [21]. The overall structure of the gated fusion is shown in Figure 4. We first adjust the dimensions of $T \in \mathbb{R}^{M \times N \times \text{hidden}}$ to $T' \in \mathbb{R}^{N \times M \times \text{hidden}}$, and through linear concatenation in the first dimension, we obtain the Catch matrix:

$$\text{Catch} = [S|T'] \in \mathbb{R}^{N \times M \times (2 \times \text{hidden})},$$

where the Catch matrix contains both temporal and spatial attention information. To explore the proportion of temporal and spatial attention in the system, we use a linear layer to extract aggregated spatiotemporal information from the Catch matrix, smoothed by the sigmoid function, to obtain the dynamic weight Gating matrix:

$$\text{Gating} = \text{Sigmoid}(\text{Linear}(\text{Catch})) \in \mathbb{R}^{N \times M \times \text{hidden}} \in (0, 1).$$

Define the matrix of aggregated spatiotemporal information features as Fusion, computed as:

$$\text{Fusion} = \text{Gating} \odot T + (1 - \text{Gating}) \odot S,$$

where \odot denotes element-wise multiplication, and $\text{Fusion} \in \mathbb{R}^{N \times M \times \text{hidden}}$. To aggregate the temporal feature dimension, we apply a linear layer to compress the last dimension's features into one dimension and perform overall dimension compression to remove the third dimension, obtaining the F matrix:

$$F = \text{squeeze}_3(\text{Linear}(\text{Fusion})) \in \mathbb{R}^{N \times M \times 1} \in \mathbb{R}^{N \times M}.$$

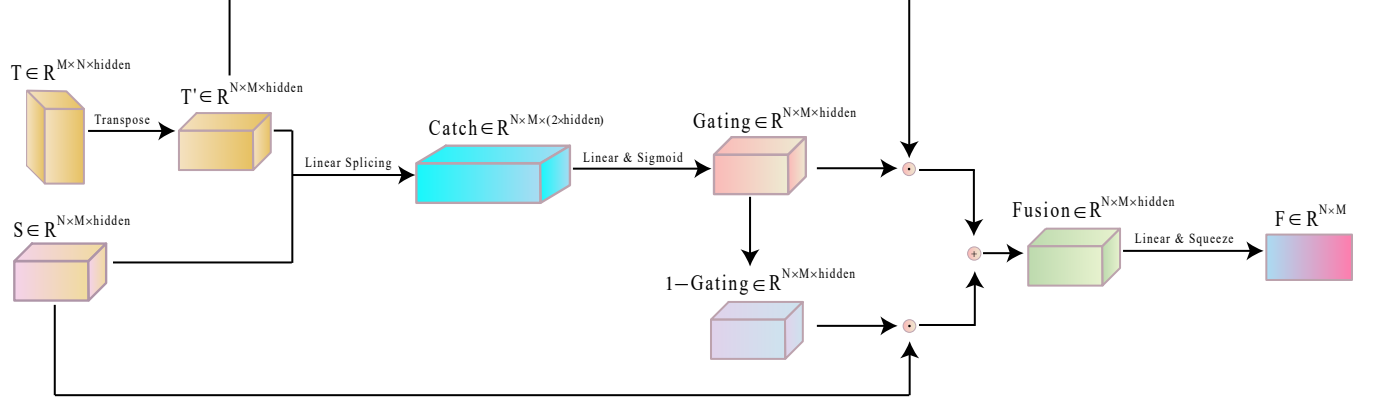


Figure 4: Fusion module architecture

3.5 DynaFC6 Network

This module implements the mapping from the spatiotemporal feature matrix $F \in \mathbb{R}^{N \times M}$ to the delayed attractor matrix $D \in \mathbb{R}^{(L+1) \times M}$ through a six-layer fully connected network (as shown in Figure 5), with the mathematical form:

$$D = \Gamma_{\text{out}} \circ \Gamma_6 \circ \dots \circ \Gamma_1(F^T).$$

In this section, we use an expansion and compression process. The first two layers expand and deepen the temporal features:

$$H_1 = \text{Dropout}(\text{ReLU}(\text{LayerNorm}(W_1 F^T + b_1))) \in \mathbb{R}^{M \times \text{hidden}},$$

$$H_2 = \text{Dropout}(\text{ReLU}(\text{LayerNorm}(W_2 H_1 + b_2))) \in \mathbb{R}^{M \times \text{hidden}},$$

In the third layer, we apply feature compression, reducing the hidden layer features to half their size:

$$H_3 = \text{Dropout}(\text{ReLU}(\text{LayerNorm}(W_3 H_2 + b_3))) \in \mathbb{R}^{M \times \text{hidden}/2}.$$

The fourth, fifth, and sixth layers maintain the hidden layer feature dimensions, with residual connections [22] added in the fourth and sixth layers to ensure gradient flow:

$$H_4 = \text{Dropout}(\text{ReLU}(\text{LayerNorm}(W_4 H_3 + b_4))) + H_3 \in \mathbb{R}^{M \times \text{hidden}/2},$$

$$H_5 = \text{Dropout}(\text{ReLU}(\text{LayerNorm}(W_5 H_4 + b_5))) \in \mathbb{R}^{M \times \text{hidden}/2},$$

$$H_6 = \text{Dropout}(\text{ReLU}(\text{LayerNorm}(W_6 H_5 + b_6))) + H_5 \in \mathbb{R}^{M \times \text{hidden}/2}.$$

Finally, through the output layer and transposition, we obtain the delayed attractor matrix:

$$O = (\text{Linear}(H_6) \in \mathbb{R}^{M \times (L+1)})^T.$$

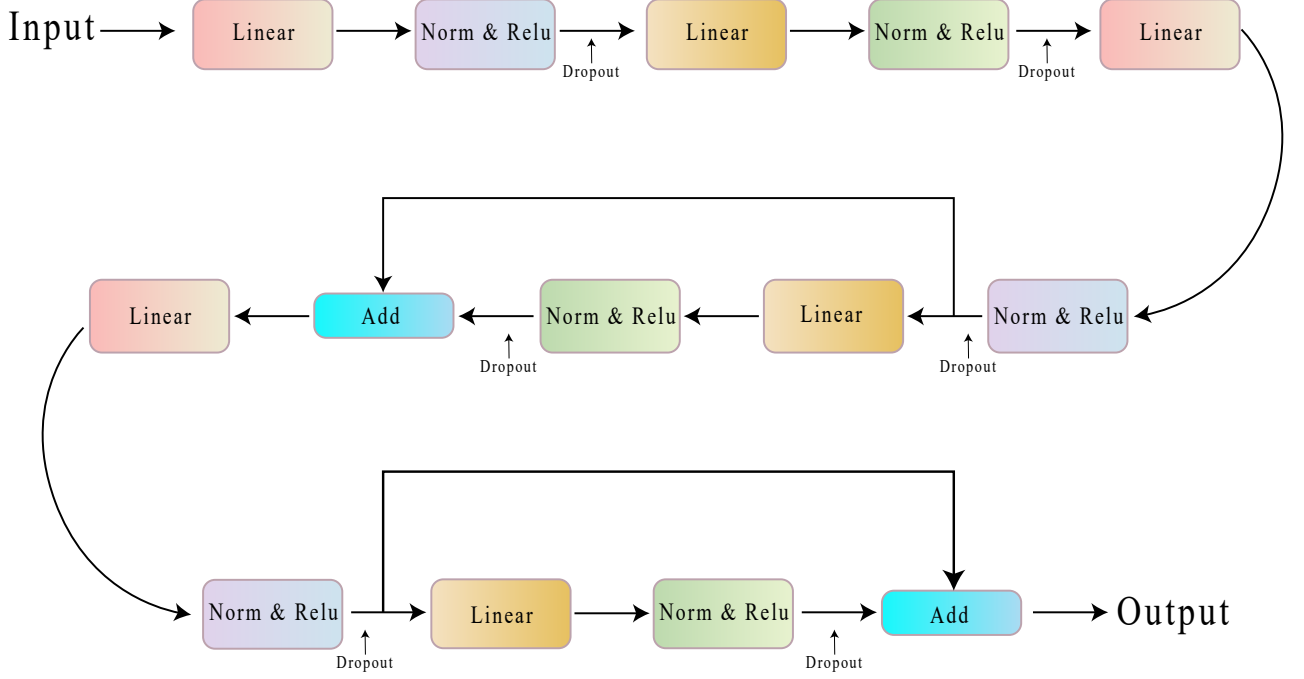


Figure 5: DynaFC6 Network architecture

4 Numerical Experiments

4.1 Dataset Generation

Consider the nondimensionalized KS equation:

$$u_t + u_{xx} + u_{xxx} + uu_x = 0.$$

Place N equally spaced points in the periodic domain $x \in [1, 16]$. The initial condition is set as:

$$u(x, 0) = \cos\left(\frac{x}{16}\right)$$

Transform the physical field to the spectral space using the Fast Fourier Transform:

$$v(k, t) = \mathcal{F}u(x, t) = \frac{1}{N} \sum_{j=1}^N u(x_j, t) e^{-ikx_j},$$

where the wavenumber k satisfies the Nyquist sampling criterion. The linear operator is defined as:

$$\mathcal{L}(k) = k^2 - k^4.$$

The fourth-order Exponential Time Differencing scheme ETD4 [23] is used to advance the time evolution, with the single-step iteration process as follows:

$$\begin{aligned} a &= e^{h\mathcal{L}/2} v_n + hQ \cdot \mathcal{N}(v_n), \\ b &= e^{h\mathcal{L}/2} v_n + hQ \cdot \mathcal{N}(a), \\ c &= e^{h\mathcal{L}/2} a + hQ \cdot (2\mathcal{N}(b) - \mathcal{N}(v_n)), \\ v_{n+1} &= e^{h\mathcal{L}} v_n + h[f_1 \mathcal{N}(v_n) + 2f_2 \mathcal{N}(a) + \mathcal{N}(b) + f_3 \mathcal{N}(c)], \end{aligned}$$

where the time step $h = \Delta t = 0.1$, and the nonlinear term is computed by decoupling in the physical space:

$$\mathcal{N}(v) = -0.5ik \cdot \mathcal{F} \left\{ [\mathcal{F}^{-1}\{v\}]^2 \right\}.$$

The key coefficients Q, f_i are calculated via contour integration in the complex plane to avoid numerical singularities:

$$Q = h \cdot \text{Re} \left(\frac{1}{M_1} \sum_r \frac{e^{h\mathcal{L}/2} - 1}{h\mathcal{L} + r} \right), \quad f_i = h \cdot \text{Re} \left(\frac{1}{M_1} \sum_r \frac{P_i(r)}{(h\mathcal{L} + r)^3} \right). \quad (i = 1, 2, 3)$$

where r represents $M_1 = 16$ equally spaced sampling points on the complex plane, and $P_i(r)$ are the ETDRK4 polynomial kernel functions. Every Δt step, the physical space solution is collected to form the dataset:

$$u(x, t) = \text{Re} [\mathcal{F}^{-1}\{v(k, t)\}].$$

To evaluate the model's performance under chaotic systems with potential real-world noise, we introduce a noise distribution to the original dataset. The Gaussian distribution is generally considered to realistically reflect real-world noise interference [24], so we add a standard normal distribution $\text{Noise} \sim N(0, 1)$, with the hyperparameter I_{noise} controlling the noise impact. The noise-affected dataset is then:

$$u(x, t)_{\text{noisy}} = u(x, t) + \text{Noise} \times I_{\text{noise}}.$$

Unless otherwise specified, we set the observation length $M = 20$ and prediction length $L = 20$.

4.2 Without Noise

To observe the model's performance under strongly nonlinear data in Kuramoto-Sivashinsky equation, we consider its performance over the time period $t \in [0, 180]$. Figure 6, Figure 7 and Figure 8 sequentially show the numerical solution of the equation, AFD-STA predictions, and absolute error for $N = 128, t \in [0, 180]$. Overall, AFD-STA maintains accurate predictions even when the equation's solution undergoes significant changes and the training and prediction data are in a 1:1 ratio. This indicates that AFD-STA has learned the dynamical characteristics of the nonlinear system.

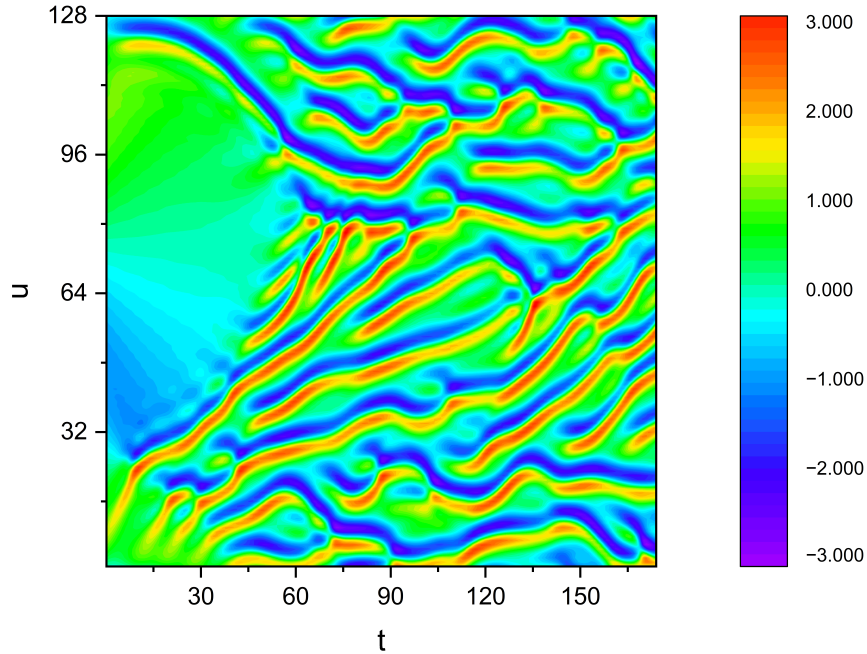


Figure 6: Numerical solution of the equation

The number of equally spaced points N significantly affects the model's performance. Generally, a larger number of equally spaced points better describes the system's overall characteristics and provides more information. Table 1 shows the results under the influence of different numbers of sampling points. We find that as the sampling interval increases, AFD-STA's performance shows an upward trend, with the best performance at $N = 128$ and stable performance at $N = 256$.

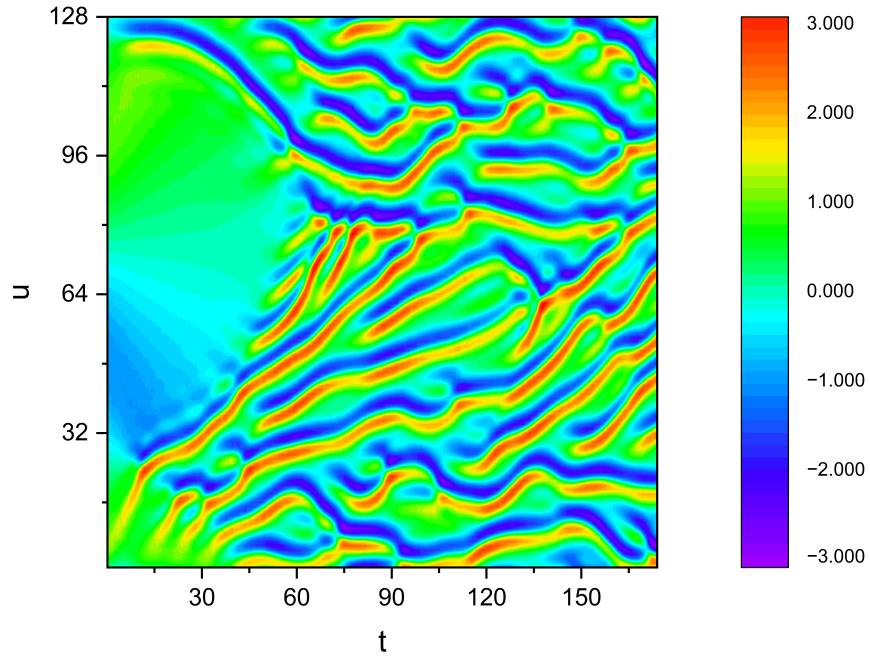


Figure 7: Prediction results for parameters $N = 128$, $t \in [0, 180]$, Noise = 0, $L = 20$, $M = 20$, with RMSE of 0.47314

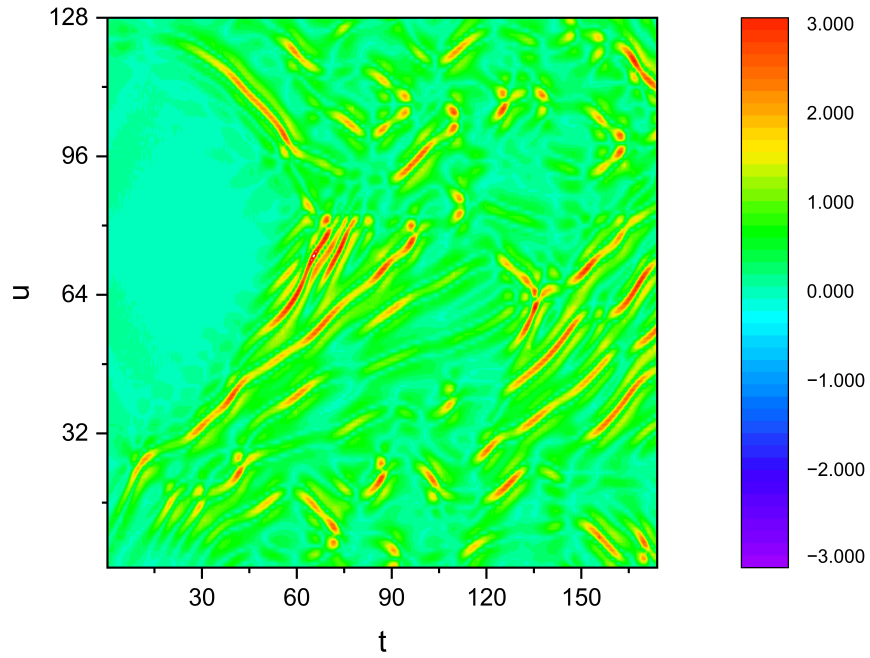


Figure 8: Absolute error between predictions and numerical solution

N	RMSE
64	0.63437
128	0.47314
256	0.49268

Table 1: Effect of different number of sampling points N on RMSE

4.3 With Noise

The previous section presented experiments without noise. However, in the real world, noise is often unavoidable due to limitations in observation techniques or uncontrollable factors. As shown in subsection 4.1, we simulate real-world noise using a standard Gaussian distribution and control the noise level with a hyperparameter.

With parameters $N = 128$, $\text{noise} = 0.10$, we evaluate the model’s performance in a time period with significant equation changes, $t \in (70, 110)$. Figure 9, Figure 10, and Figure 11 sequentially show the numerical solution of the equation, model predictions, and absolute error under these parameters. We find that even in a strongly nonlinear variation interval with noise interference, our model maintains accurate predictions, with larger errors only at a few individual points, demonstrating the model’s robust performance.

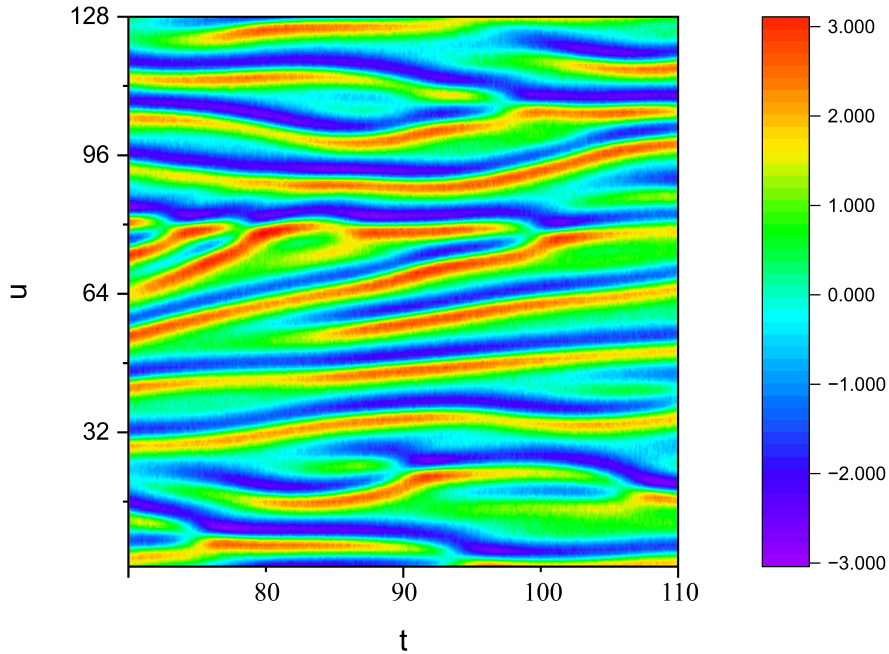


Figure 9: Numerical solution of the equation under noise interference

To test the impact of noise on our model, we conducted comparative experiments. In typical data application scenarios, the greater the noise interference, the more difficult it is to accurately predict the data. As shown in Table 2, as the noise parameter gradually increases, the model’s prediction performance shows a declining trend.

4.4 Ablation Experiment

To verify whether each component contributes to the model and to what extent, we designed ablation experiments by sequentially removing each component. With parameters $N = 128$, $L = 20$, $M = 20$, $\text{Noise} = 0.2$, single-step predictions are performed in the region $t \in (120, 122)$. Our model consists of four components: Adap-EWMA, Spatiotemporal Attention, Fusion, and DynaFC6. In each experiment, we fix the other three components, and if

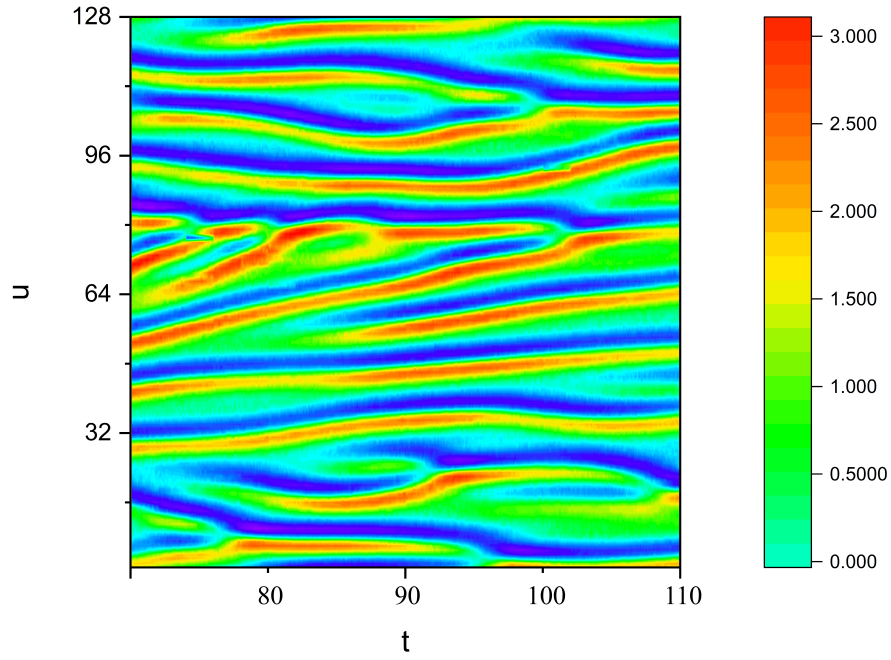


Figure 10: Prediction results for parameters $N = 128, t \in [70, 110]$, Noise = 0.1, $L = 20, M = 20$, with RMSE of 0.55742

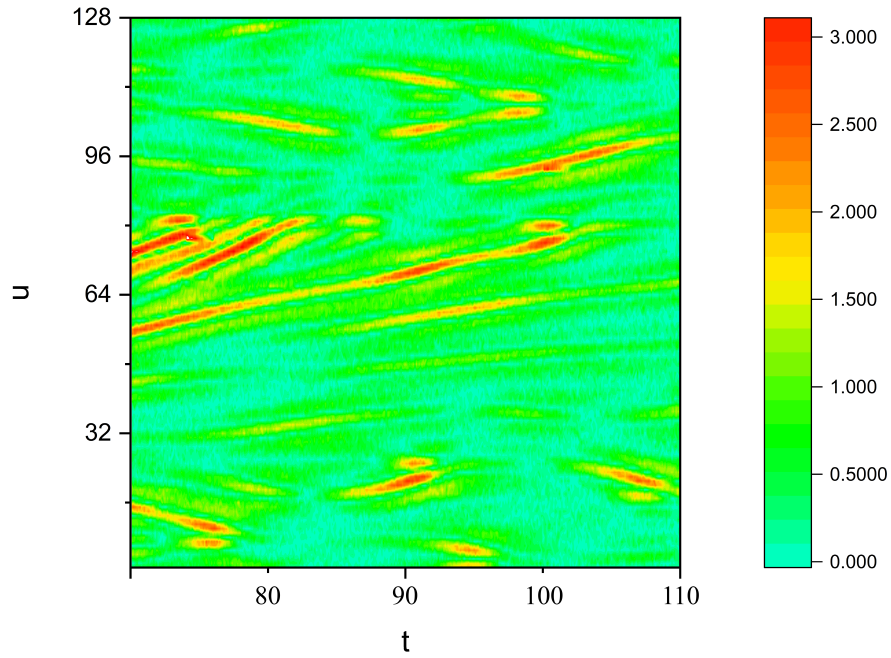


Figure 11: Absolute error between predictions and numerical solution under noise interference

Noise	RMSE
0	0.53383
0.1	0.55742
0.15	0.58342
0.2	0.61992

Table 2: Effect of different noise parameters on RMSE

removing the current component reduces the model’s prediction accuracy, it indicates that the component has a positive effect on the model. Since FC-6 handles the task of dimension adjustment, removing it directly prevents obtaining the corresponding attractor, so we replace it with a simple linear layer. As shown in Table 3, each component of the model contributes positively to the final performance, with the Spatiotemporal Attention module contributing the most.

Component	Choice				
Adpa-EWMA	✓		✓	✓	✓
Spatiotemporal Attention	✓	✓		✓	✓
Fusion	✓	✓	✓		✓
DynaFC-6	✓	✓	✓	✓	
RMSE	0.38286	0.40698	0.41729	0.39357	0.39845

Table 3: Ablation study of different components

The experiments show that removing the Spatiotemporal Attention mechanism leads to the largest performance loss, with RMSE increasing by 9.0% ($\Delta = 0.034$) relative to the baseline. The absence of the gated fusion module increases RMSE by 6.8%, while removing the adaptive EWMA and replacing the FC-6 layer cause performance degradations of 6.3% and 4.0%, respectively. Notably, the complete model (Baseline) has an RMSE of 0.383, significantly lower than the worst value (0.417) when individual components are removed, with a performance improvement ($\Delta = 0.034$) exceeding 50% of the sum of individual component contributions, indicating a positive synergistic effect between modules.

4.5 Comparisons Experiment

Our model demonstrates accurate prediction performance in both noise-free and noisy datasets. To evaluate our model’s performance against other outstanding models, we select parameters $N = 128$, $L = 20$, $M = 20$, Noise = 0.2, $t_{\text{gap}} = 0.1$, and perform single-step predictions in the region $t \in (120, 122)$ in Kuramoto-Sivashinsky equation. As shown in Table 4, our model exhibits a significant advantage over other models across various metrics.

On the other hand, similar to the Kuramoto-Sivashinsky equation, the Brusselator equation and the Swift-Hohenberg equation are widely used nonlinear reaction-diffusion models, encompassing rich dynamical behaviors. To test whether AFD-STA outperforms other models in other nonlinear systems, we conduct experiments on the Brusselator equation and the Swift-Hohenberg equation. As shown in Table 5 and Table 6, we find that AFD-STA performs the best across various metrics. LSTM [25] and XGBoost [26] are widely used in time series tasks and achieved good results in this prediction task.

Phase space reconstruction techniques, by constructing the original attractor and delayed attractor, integrate temporal variation relationships and spatial geometric features. The i -th row of the delayed attractor $Z(t_i) = [x_k(t_i), x_k(t_{i+1}), \dots, x_k(t_{i+M-1})] \in \mathbb{R}^M$ can be regarded as the result of predicting $i - 1$ steps based on the original attractor O . Thus, we believe that $L + 1$ predictions enable the model to incorporate more original information, uncovering relationships in time series changes. Additionally, since the $L + 1$ predictions are considered relatively independent, and the final result evaluation uses each predicted time step, this reduces model overfitting while enhancing robustness, minimizing unstable performance due to noise interference in specific cases.

Model	RMSE	MAE	SAMPE	MAD
AFD-STA	0.46846	0.41038	57.89778	0.18107
LSTM	0.50263	0.43640	58.83854	0.21419
XGBoost	0.49507	0.43183	60.00500	0.19873
CNN	0.54222	0.47550	64.71703	0.21977
DNN	0.65152	0.57656	65.44706	0.24855
Dlinear	1.01890	0.93453	117.15215	0.29549

Table 4: Single-step prediction of Kuramoto-Sivashinsky equation with parameters $N = 128$, $t_{\text{start}} = 120$, $L = 20$, $M = 20$, $t_{\text{gap}} = 0.1$, Noise = 0.2.

Model	RMSE	MAE	SAMPE	MAD
AFD-STA	0.23778	0.19341	50.83187	0.15899
LSTM	0.27289	0.22177	52.06842	0.19161
XGBoost	0.26578	0.21511	55.47640	0.17562
CNN	0.28124	0.22733	58.94235	0.17178
DNN	0.38313	0.33157	85.43416	0.15879
Dlinear	0.48980	0.43149	114.65781	0.18528

Table 5: Single-step prediction of Brusselator equation with parameters $N = 128$, $t_{\text{start}} = 0.1$, $L = 20$, $M = 20$, $t_{\text{gap}} = 0.00001$, Noise = 0.2.

Model	RMSE	MAE	SAMPE	MAD
AFD-STA	0.23695	0.19338	81.76329	0.15645
LSTM	0.27888	0.22513	90.01469	0.18522
XGBoost	0.27282	0.22116	88.75923	0.17777
CNN	0.26262	0.21159	89.92485	0.16986
DNN	0.27962	0.22765	94.41591	0.18603
Dlinear	0.31240	0.25400	106.24605	0.18757

Table 6: Single-step prediction of Swift-Hohenberg equation with parameters $N = 128$, $t_{\text{start}} = 5$, $L = 20$, $M = 20$, $t_{\text{gap}} = 0.001$, Noise = 0.2.

5 Conclusion

The proposed AFD-STA framework breaks through traditional methods' dependence on initial conditions, directly learning intrinsic dynamical characteristics of spatiotemporal chaotic systems from observational data through phase space reconstruction for prediction. This method only requires training data equivalent to the prediction duration (1:1 ratio), achieving high-precision predictions in canonical systems including Kuramoto-Sivashinsky, Brusselator, and Swift-Hohenberg. Compared with other models, AFD-STA maintains stable performance under Gaussian noise interference with $\sigma \leq 0.2$.

The current AFD-STA architecture still has limitations in long-term predictions of attractor mutations, primarily stemming from the time-varying characteristics of Lyapunov exponent spectra in infinite-dimensional spatiotemporal chaotic systems. Our AFD-STA network can only focus on situations with stable attractor properties in the short term, and cannot predict attractor mutations during long-term predictions. This limitation may originate from insufficient

attention to the dynamic evolution trends of attractors. Future work plans to introduce the Brox variational optical flow method [27], capturing attractor deformation trends by quantifying velocity field changes between consecutive time steps, thereby constructing an optical flow-spatiotemporal joint attention mechanism to enhance modeling capabilities for dynamic evolution of phase space structures.

Acknowledgement

This research is supported by the Shandong Natural Science Foundation (ZR2024QD287).

References

- [1] Heinz Georg Schuster and Wolfram Just. *Deterministic chaos: an introduction*. John Wiley & Sons, 2006.
- [2] Edward N Lorenz. Deterministic nonperiodic flow 1. In *Universality in Chaos, 2nd edition*, pages 367–378. Routledge, 2017.
- [3] David Ruelle. *Turbulence, strange attractors and chaos*, volume 16. World Scientific, 1995.
- [4] Guanrong Chen and Tetsushi Ueta. Yet another chaotic attractor. *International Journal of Bifurcation and chaos*, 9(07):1465–1466, 1999.
- [5] Gi Siv Ashinsky. Nonlinear analysis of hydrodynamic instability in laminar flames—i. derivation of basic equations. In *Dynamics of Curved Fronts*, pages 459–488. Elsevier, 1988.
- [6] Jack Swift and Pierre C Hohenberg. Hydrodynamic fluctuations at the convective instability. *Physical Review A*, 15(1):319, 1977.
- [7] Ilya Prigogine and René Lefever. Symmetry breaking instabilities in dissipative systems. ii. *The Journal of Chemical Physics*, 48(4):1695–1700, 1968.
- [8] Claudio Canuto, M Yousuff Hussaini, Alfio Quarteroni, and Thomas A Zang. *Spectral methods: evolution to complex geometries and applications to fluid dynamics*. Springer Science & Business Media, 2007.
- [9] William H Press. *Numerical recipes 3rd edition: the art of scientific computing*. Cambridge university press, 2007.
- [10] George Em Karniadakis, Ioannis G Kevrekidis, Lu Lu, Paris Perdikaris, Sifan Wang, and Liu Yang. Physics-informed machine learning. *Nature Reviews Physics*, 3(6):422–440, 2021.
- [11] Wei Cheng, Yan Wang, Zheng Peng, Xiaodong Ren, Yubei Shuai, Shengyin Zang, Hao Liu, Hao Cheng, and Jiagui Wu. High-efficiency chaotic time series prediction based on time convolution neural network. *Chaos, Solitons & Fractals*, 152:111304, 2021.
- [12] Hao-Chang Chen and Du-Qu Wei. Chaotic time series prediction using echo state network based on selective opposition grey wolf optimizer. *Nonlinear Dynamics*, 104(4):3925–3935, 2021.
- [13] Hatice Vildan Dudukcu, Murat Taskiran, Zehra Gulru Cam Taskiran, and Tulay Yildirim. Temporal convolutional networks with rnn approach for chaotic time series prediction. *Applied Soft Computing*, 133:109945, 2023.
- [14] Hamid Nasiri and Mohammad Mehdi Ebadzadeh. Mfrfnn: multi-functional recurrent fuzzy neural network for chaotic time series prediction. *Neurocomputing*, 507:292–310, 2022.
- [15] Seçkin Karasu and Aytaç Altan. Crude oil time series prediction model based on lstm network with chaotic henry gas solubility optimization. *Energy*, 242:122964, 2022.
- [16] Floris Takens. Detecting strange attractors in turbulence. In *Dynamical Systems and Turbulence, Warwick 1980: proceedings of a symposium held at the University of Warwick 1979/80*, pages 366–381. Springer, 2006.
- [17] Ethan R Deyle and George Sugihara. Generalized theorems for nonlinear state space reconstruction. *Plos one*, 6(3):e18295, 2011.
- [18] Chuan Chen, Rui Li, Lin Shu, Zhiyu He, Jining Wang, Chengming Zhang, Huanfei Ma, Kazuyuki Aihara, and Luonan Chen. Predicting future dynamics from short-term time series using an anticipated learning machine. *National Science Review*, 7(6):1079–1091, 2020.
- [19] Ramazan Gençay, Faruk Selçuk, and Brandon J Whitcher. *An introduction to wavelets and other filtering methods in finance and economics*. Elsevier, 2001.
- [20] Ashish Vaswani, Noam Shazeer, Niki Parmar, Jakob Uszkoreit, Llion Jones, Aidan N Gomez, Łukasz Kaiser, and Illia Polosukhin. Attention is all you need. *Advances in neural information processing systems*, 30, 2017.

- [21] Noam Shazeer, Azalia Mirhoseini, Krzysztof Maziarczyk, Andy Davis, Quoc Le, Geoffrey Hinton, and Jeff Dean. Outrageously large neural networks: the sparsely-gated mixture-of-experts layer. *arXiv preprint arXiv:1701.06538*, 2017.
- [22] Kaiming He, Xiangyu Zhang, Shaoqing Ren, and Jian Sun. Deep residual learning for image recognition. In *Proceedings of the IEEE Conference on Computer Vision and Pattern Recognition*, pages 770–778, 2016.
- [23] Steven M Cox and Paul C Matthews. Exponential time differencing for stiff systems. *Journal of Computational Physics*, 176(2):430–455, 2002.
- [24] William A Gardner and Enders A Robinson. Statistical spectral analysis—a nonprobabilistic theory. 1989.
- [25] Sepp Hochreiter and Jürgen Schmidhuber. Long short-term memory. *Neural Computation*, 9(8):1735–1780, 1997.
- [26] Tianqi Chen and Carlos Guestrin. Xgboost: A scalable tree boosting system. In *Proceedings of the 22nd Acm Sigkdd International Conference on Knowledge Discovery and Data Mining*, pages 785–794, 2016.
- [27] Thomas Brox and Jitendra Malik. Large displacement optical flow: descriptor matching in variational motion estimation. *IEEE Transactions on Pattern Analysis and Machine Intelligence*, 33(3):500–513, 2010.